energies

Article

Thermohydraulic Performance and Entropy Generation of a Triple-Pass Solar Air Heater with Three Inlets

Nguyen Minh Phu [1,*], Ngo Thien Tu [2,3] and Nguyen Van Hap [2,3]

[1] Faculty of Heat and Refrigeration Engineering, Industrial University of Ho Chi Minh City (IUH), 12 Nguyen Van Bao, Go Vap District, Ho Chi Minh City 700000, Vietnam
[2] Faculty of Mechanical Engineering, Ho Chi Minh City University of Technology (HCMUT), 268 Ly Thuong Kiet, District 10, Ho Chi Minh City 700000, Vietnam; ngothientu@hcmut.edu.vn (N.T.T.); nguyenvanhap@hcmut.edu.vn (N.V.H.)
[3] Vietnam National University, Linh Trung Ward, Thu Duc District, Ho Chi Minh City 700000, Vietnam
* Correspondence: nguyenminhphu@iuh.edu.vn; Tel.: +84-906-929-498

Abstract: In this paper, a triple-pass solar air heater with three inlets is analytically investigated. The effects of airflow ratios of the second and third passes (ranging from 0 to 0.4), and the Reynolds number of the third pass (ranging from 8000 to 18,000) on the thermohydraulic efficiency and entropy generation are assessed. An absorber plate equipped with rectangular fins on both sides is used to enhance heat transfer. The air temperature change in the passes is represented by ordinary differential equations and solved by numerical integration. The results demonstrate that the effect of the third pass airflow ratio on the thermohydraulic efficiency and entropy generation is more significant than that of the second pass airflow ratio. The difference in air temperature through the collector shows an insignificant reduction, but the air pressure loss is only 50% compared with that of a traditional triple-pass solar air heater. Increasing the air flow ratios dramatically reduces entropy generation. Multi-objective optimization found a Reynolds number of 11,156 for both the airflow ratio of the second pass of 0.258 and airflow ratio of the third pass of 0.036 to be the an optimal value to achieve maximum thermohydraulic efficiency and minimum entropy generation.

Keywords: multiple pass heat exchanger; solar air heater; thermohydraulic efficiency; Pareto front; flow ratio

Citation: Phu, N.M.; Tu, N.T.; Hap, N.V. Thermohydraulic Performance and Entropy Generation of a Triple-Pass Solar Air Heater with Three Inlets. *Energies* **2021**, *14*, 6399. https://doi.org/10.3390/en14196399

Academic Editor: Efstathios E. Michaelides

Received: 4 September 2021
Accepted: 4 October 2021
Published: 7 October 2021

1. Introduction

Hot air is an essential source of thermal energy for industrial fields such as regarding drying, pre-heating of bottles, textile production processes, painting processes, and conditioning tobacco. For moderate-temperature heating, a solar air heater (SAH) can be employed, which reduces fossil fuel energy consumption [1]. SAHs are the simplest energy conversion devices, as they can be made from locally available materials. However, SAHs reveal some limitations that arise from the heat transfer fluid of air, which cannot be stored as hot water can, and the low convection heat transfer coefficient of air. Heat transfer improvement between the airflow and absorption plate of a SAH is a topic of constant interest to researchers. Inserts including rib roughness, fins, porous media, or baffles in the SAH duct have led to increases in the heat transfer rate due to the elimination of the laminar sub-layer close to the absorber plate and airflow reconfiguration [2,3]. The small convection heat transfer coefficient of the air leads to a high absorber plate temperature, resulting in a large top heat loss of the SAH. To reduce this heat loss, airflow with multiple passes is structured such that the air receives heat from both sides of the absorber plate, glass, and back plate. [4,5]. Tuncer et al. [6] used triple and quadruple-pass SAHs to dry food. They reported that pressure losses of 3.8 and 4.5 Pa were obtained for triple and quadruple-pass SAHs, respectively. In addition, air temperature increases of 18.2 and 20.1 °C were observed in the triple and quadruple-pass SAHs, respectively.

Khanlari et al. [7] dried municipal sewage sludge using triple and quadruple-pass SAHs. A V-groove absorber plate was designed to enhance heat transfer. Their experimental results proved that the collector efficiency can be up to 81.7%. Potato drying using a triple-pass SAH has been experimentally examined by Kesavan et al. [8]. A wire mesh in the second pass and sand as a thermal storage medium were adopted in order to increase the heat transfer rate and extend the drying time. The highest thermal and exergy efficiencies of 66% and 87%, respectively, were deduced. Sopian et al. [9] discussed a double-pass solar collector with porous media in the second pass. They confirmed that the collector had a higher thermal efficiency compared to that of a single-pass SAH.

Another modification to multi-pass SAHs is the adjustment of the air flow in each channel by recycling flow or adding air inlets. This correction can improve collector performance, as the multi-pass air collector has a large pressure loss and the temperature difference between the fluid and the surface in each channel differs. Table 1 summarizes studies on the flow patterns changed in the multi-pass SAHs. Ho et al. [10] explored a double-pass SAH with recycled flow. Wire mesh, as a heat transfer enhancement media, was inserted in the channel between the absorber plate and back plate. They reported an optimal recycle ratio of 1.0 to obtain the highest collector efficiency improvement. Yeh and Ho [11] divided the space between the absorber plate and back plate into two air channels. Longitudinal fins were attached to the absorber plate in order to intensify the heat exchange. They concluded that the collector efficiency can be improved through an increase in the reflux ratio. Singh and Dhiman [12] added wire mesh packing in the main air channel between a glass cover and absorber plate. The recycle ratio of 1.8 yielded the largest thermohydraulic efficiency. Ho et al. [13] utilized corrugated absorber and back plates to improve heat transfer in a double-pass SAH with recycled flow. It was shown that the thermal performance improved with an increasing recycle ratio and decreasing air flow rate. The optimum recycle ratio of 0.5 was found considering the trade-off of heat transfer improvement and pressure loss penalty. Abo-Elfadl et al. [14] recently added an air inlet port in the second pass of a double-pass SAH. The absorber plate was equipped with pin fins for heat transfer augmentation. They confirmed that 66.7% of the air supply at the port led to the highest energy and exergy efficiencies. More recently, Ahmadkhani et al. [15] investigated two flow configurations, including recycled flow to the back plate or upper glass cover. A packed bed matrix was utilized in the main air channel to perform the parametric study. It was identified that the recycled flow to the back plate led to a higher air temperature rise.

Table 1. Summary of multi-pass SAH studies on flow pattern change.

Investigators (Year)	Flow Pattern	Heat Transfer Enhancement	Main Finding
Ho et al., 2013 [10]		Wire mesh	Optimal recycle ratio of 1.0
Yeh and Ho, 2013 [11]	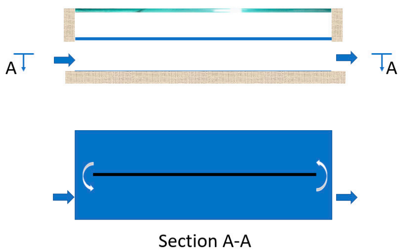	Longitudinal fin	Collector efficiency increased with recycle ratio

Table 1. *Cont.*

Investigators (Year)	Flow Pattern	Heat Transfer Enhancement	Main Finding
Singh and Dhiman, 2018 [12]		Wire mesh packing	Optimal recycle ratio of 1.8
Ho et al., 2018 [13]		Corrugated absorber and back plates	Optimal recycle ratio of 0.5
Abo-Elfadl et al., 2020 [14]		Pin fin	In total, 66.7% of air supply at the second pass exhibited the highest energy and exergy efficiencies
Ahmadkhani et al., 2021 [15]	 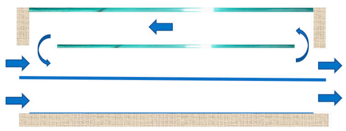	Packed bed matrix	Recycle flow to back plate (upper figure) led to higher air temperature rise

The above literature review indicates that multiple passes and various air flows within the passes can improve the thermohydraulic performance of an SAH. However, a study for triple-pass SAHs with air flow modification was not found. Furthermore, studies focused on the parameters related to the second law of thermodynamics are lacking. In this study, a triple-pass SAH with three inlets each at an air pass is investigated. The main aim of the present study was to determine the flow rate of each pass such that the collector efficiency can be augmented and the entropy generation lowered.

2. Model Description

The schematic diagram of a three-inlet triple-pass air collector is shown in Figure 1. In this study, the collector dimensions are fixed, including the collector length L, width W, and depth of an air channel D. The collector includes two glass covers, one absorber plate, and one back plate. The air travels through the surfaces in turn, forming three passes. Each pass has an air inlet with ambient temperature T_a, as shown in the figure. The air flow through the third pass is the total flow, with the mass flow rate $\dot{m}$. Let y and z be the additional air fractions supplied to passes 2 and 3, respectively. The air fraction through the first pass is $(1 - y - z)$. The two sides of the absorber plate was equipped with longitudinal fins in order to enhance the heat transfer for the plate. The mathematical model is established with the following assumptions:

- The flow in a channel is considered one-dimensional in the x-direction.
- The flow is steady and the air fluid is incompressible.
- The thermophysical properties of the air and the SAH are temperature-independent; and
- The bottom plate and the edges of the SAH are perfectly insulated from the surrounding environment.

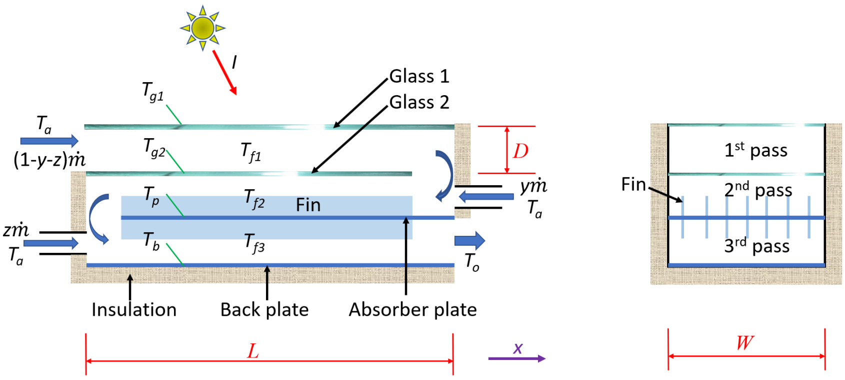

Figure 1. Triple-pass solar air heater with three inlets and notation.

The heat balance equation for the glass, plates, and air in the three channels is as follows:

- Glass 1: Solar irradiation absorbed by the glass balances the heat exchanged by convection and radiation from the top and bottom sides of the glass [4,16]:

$$I\alpha_{g1} + h_w(T_a - T_{g1}) + h_{r,a}\left(T_{sky} - T_{g1}\right) + h_{r,g1,g2}(T_{g2} - T_{g1}) + h_{f1,g1}\left(T_{f1} - T_{g1}\right) = 0, \quad (1)$$

where the sky temperature is calculated by $T_{sky} = 0.0552{T_a}^{1.5}$.

- The heat gain of first pass air in an infinitesimal change (dx) is equal to the heat exchange by convection with glasses 1 and 2 as:

$$(1 - y - z)\dot{m}c_p dT_{f1} = \left[Wh_{f1,g1}\left(T_{g1} - T_{f1}\right) + Wh_{f1,g2}\left(T_{g2} - T_{f1}\right)\right]dx. \quad (2)$$

Therefore, the variation in the first pass air temperature along the x-direction due to the convection heat transfer of the air with the two glasses is expressed as follows:

$$\frac{dT_{f1}}{dx} = \frac{Wh_{f1,g1}\left(T_{g1} - T_{f1}\right) + Wh_{f1,g2}\left(T_{g2} - T_{f1}\right)}{(1 - y - z)\dot{m}c_p}. \quad (3)$$

- Similarly, for glass 2:

$$I\tau_{g1}\alpha_{g2} + h_{f1,g2}(T_{f1} - T_{g2}) + h_{f2,g2}(T_{f2} - T_{g2}) + h_{r,g1,g2}(T_{g1} - T_{g2}) + h_{r,g2,p1}(T_{p1} - T_{g2}) = 0. \quad (4)$$

- Similar to the change of the first pass air temperature, the air in the second pass exchanges heat with glass 2 and receives thermal energy by convection with the finned absorber plate. The convection heat transfer of the air with the fins and their prime surface is calculated through the temperature difference of the absorber plate (T_p) and the air (T_{f2}) with the fin efficiency. Hence, the change in the second pass air temperature can be written as:

$$\frac{dT_{f2}}{dx} = \frac{Wh_{f2,g2}\left(T_{g2} - T_{f2}\right) + Wh_{f2,p}\phi\left(T_p - T_{f2}\right)}{(1 - z)\dot{m}c_p}, \quad (5)$$

where ϕ is the area-weighted fin efficiency.

- The absorber plate can be expressed as:

$$I\tau_{g1}\tau_{g2}\alpha_p + h_{f2,p}\phi(T_{f2} - T_p) + h_{r,g2,p}(T_{g2} - T_p) + h_{f3,p}\phi(T_{f3} - T_{p1}) + h_{r,b,p}(T_b - T_p) = 0. \quad (6)$$

- The change in the third pass air temperature can be expressed as:

$$\frac{dT_{f3}}{dx} = \frac{Wh_{f3,p}\Phi\left(T_p - T_{f3}\right) + Wh_{f3,b}\left(T_b - T_{f3}\right)}{\dot{m}c_p}. \tag{7}$$

- The back plate-received radiation heat transfer from the absorber plate and transfer heat to the third pass air by convection is expressed as:

$$h_{f3,b}\left(-T_{f3} + T_b\right) + h_{r,b,p}\left(T_b - T_p\right) = 0. \tag{8}$$

Boundary conditions for the ordinary differential Equations (2), (4) and (6) are as follows:

The temperature of the air entering the first pass ($T_{f1(x=0)}$) is equal to the ambient temperature (T_a):

$$T_{f1(x=0)} = T_a. \tag{9a}$$

- The air entering the second pass with a flow fraction $(1 - z)$ is a mixture of the air exiting the first pass with the flow fraction $(1 - y - z)$ and the air from the second inlet with the flow fraction (y). The mixing temperature is calculated from the mass-weighted average as follows:

$$T_{f2(x=L)} = [(1 - y - z)T_{f1(x=L)} + yT_a]/(1 - z). \tag{9b}$$

- Similarly, the temperature boundary condition for the air entering the third pass can also be expressed as:

$$T_{f3(x=0)} = (1 - z)T_{f2(x=0)} + zT_a. \tag{9c}$$

The radiative heat transfer coefficient in the above system of equations can be evaluated through the following:

- Radiation from glass 1 to the surroundings:

$$h_{r,a} = \sigma\varepsilon_{g1}\left({T_{g1}}^2 + {T_{sky}}^2\right)\left(T_{g1} + T_{sky}\right); \tag{10}$$

- Radiation of glasses:

$$h_{r,g1,g2} = \sigma\left({T_{g1}}^2 + {T_{g2}}^2\right)\frac{T_{g1} + T_{g2}}{1/\varepsilon_{g1} + 1/\varepsilon_{g2} - 1}; \tag{11}$$

- Radiation of glass 1 and the absorber plate:

$$h_{r,g2,p} = \sigma\left({T_{g2}}^2 + {T_p}^2\right)\frac{T_{g2} + T_p}{1/\varepsilon_{g2} + 1/\varepsilon_p - 1}; \text{ and} \tag{12}$$

- Radiation of the absorber plate and back plate:

$$h_{r,b,p} = \sigma\left({T_b}^2 + {T_p}^2\right)\frac{T_b + T_p}{1/\varepsilon_b + 1/\varepsilon_p - 1}. \tag{13}$$

The convective heat transfer coefficient of the air in the ducts can be estimated from the empirical correlation. The correlation was developed for the rectangular solar heater duct in the thermally developing flow [17] and has been adopted by many studies on solar air heater ducts [18–20].

$$h_{f1,g1} = h_{f1,g2} = 0.018Re_1^{0.8}Pr^{0.4}k/D_e, \tag{14a}$$

$$h_{f2,g2} = h_{f2,p} = 0.018Re_2^{0.8}Pr^{0.4}k/D_e, \tag{14b}$$

$$h_{f3,p} = h_{f3,p} = 0.018Re_3^{0.8}Pr^{0.4}k/D_e, \tag{14c}$$

where Pr and D_e are the Prandtl number and hydraulic diameter of the air duct, respectively, and Re_1, Re_2, and Re_3 are the respective Reynolds numbers in passes 1, 2, and 3. These quantities are defined by:

$$Re_1 = \rho D_e V_1/\mu, \tag{15a}$$

$$Re_2 = \rho D_e V_2/\mu, \tag{15b}$$

$$Re_3 = \rho D_e V_3/\mu, \tag{15c}$$

$$Pr = \mu c_p/k, \tag{16}$$

$$D_e = \frac{4WD}{2(W+D)}. \tag{17}$$

The wind loss heat transfer coefficient for glass 1 can be determined using the McAdams formula [21]:

$$h_w = 5.7 + 1.2V_w. \tag{18}$$

The area-weighted fin efficiency can be estimated as [11,18,19]:

$$\phi = 1 + \left(A_f/A_c\right)\eta_f, \tag{19}$$

where A_f is the total surface area of the fins and A_c is the collector surface area with $A_f = 2nW_fL$ and $A_c = LW$, in which n and W_f are the number of fins and fin height, respectively.

The fin efficiency is defined as:

$$\eta_f = \frac{tanh\left(MW_f\right)}{MW_f}, \tag{20}$$

where $M = \sqrt{2\frac{h_{f1,g1}}{k_s t}}$, in which t and k_s are the fin thickness and thermal conductivity of the fin, respectively.

The air mass flow rate ($\dot{m}$) and air velocity (V) have the following relations:

- For the first pass,

$$(1-y-z)\dot{m} = WD\rho V_1; \tag{21a}$$

- for the second pass,

$$(1-y)\dot{m} = WD\rho V_2; \text{ and} \tag{21b}$$

- for the third pass,

$$\dot{m} = WD\rho V_3. \tag{21c}$$

The useful heat gain is determined from the air temperature difference of the collector as follows:

$$Q = \dot{m}c_p(T_o - T_a). \tag{22}$$

The air pumping power can be calculated by:

$$P_{flow} = \dot{m}\frac{\Delta P}{\rho}, \tag{23}$$

where ΔP is the air pressure difference through the collector, which sums the pressure drops of passes, as expressed by:

$$\Delta P = 2\rho f_1 V_1^2 \frac{L}{D_e} + 2\rho f_2 V_2^2 \frac{L}{D_e} + 2\rho f_3 V_3^2 \frac{L}{D_e}. \tag{24}$$

The friction factor of each pass is given as [17,18]:

$$f_1 = 0.079Re_1^{-0.25}, \tag{25a}$$

$$f_2 = 0.079 Re_2^{-0.25}, \text{ and} \tag{25b}$$

$$f_3 = 0.079 Re_3^{-0.25}. \tag{25c}$$

Therefore, the thermohydraulic efficiency is defined as:

$$\eta_{eff} = \frac{Q - P_{flow}/C_o}{LWI}, \tag{26}$$

where C_o is the conversion factor of the mechanical work to heat (C_o = 0.2) [4,22].

Entropy generation of a SAH exists as a result of irreversibility. The irreversibility may consist of the absorption of radiation by the absorber plate, heat transfer to the working air, heat loss to the environment, and frictional loss of the working air. The entropy generation can be determined using the entropy balance for a steady control volume without work transfer [23,24]:

$$S_{gen} = (1/T_a - 1/T_s)Q_s + [ln(T_o/T_a) - T_o/T_a + 1]\dot{m}c_p - \dot{m}Rln\left(\frac{P_a}{P_a + \Delta P}\right), \tag{27}$$

where T_s is the solar temperature (T_s = 5777 K) and Q_s is the solar energy absorbed by the absorber plate ($Q_s = I(\tau\alpha)LW$).

The parameters used as input for the mathematical model are reported in Table 2. Most of the parameters were obtained from the study of Ramani et al. [16] for the sake of validating numerical computation in the present study. The thermophysical parameters of air were estimated at ambient temperature. Temperature gradient equations—that is, Equations (3), (5) and (7)—can be solved by numerical integration in the form of Equation (28) [25]. The code for the solution of the governing equations was implemented in the software EES [26] using the built-in integral function. The details of the solution procedure are presented in the textbook of Nellis and Klein [27]. Figure 2 shows a comparison of the air temperature distribution in a double-pass solar air collector. There is good agreement between the results obtained in this study and the published results. Thus, the formulation of the governing equations and solution strategy can ensure accuracy of the results.

$$\Delta T = \int_0^L \frac{dT_f}{dx} \mathrm{d}x. \tag{28}$$

Table 2. Input parameters.

Parameter	Value	Reference
Thermal conductivity of fin	k_s = 50.2 $\mathrm{Wm^{-1}K^{-1}}$	[19]
Fin thickness	t = 0.95 mm	[19]
Number of fins	n = 20	-
Fin height	W_f = 10 mm	-
Collector length	L = 2.1 m	[16]
Collector width	W = 0.54 m	[16]
Collector depth	D = 0.021 m	[16]
Solar radiation	I = 848 $\mathrm{W/m^2}$	[16]
Ambient temperature	T_a = 27 °C	[16]
Absorptivity of glass covers	$\alpha_{\gamma1} = \alpha_{\gamma2} = 0.05$	[16]
Absorptivity of absorber plate	$\alpha_\pi = 0.92$	[16]
Emissivity of glass covers	$\varepsilon_{\gamma1} = \varepsilon_{\gamma2} = 0.92$	[16]
Emissivity of absorber plate	$\varepsilon_\pi = 0.92$	[16]
Emissivity of back plate	$\varepsilon_\beta = 0.92$	-
Transmissivity of glass covers	$\tau_{\gamma1} = \tau_{\gamma2} = 0.84$	[19]
Effective transmittance–absorptance product	$\tau\alpha = 0.78$	[28]
Wind velocity	V_w = 1 m/s	-
Increment in x-coordinate	$\Delta\xi$ = 0.21 μ	-
Stefan's constant	$\sigma = 5.67\cdot10^{-8}\ \Omega/(\mu^2K^4)$	-

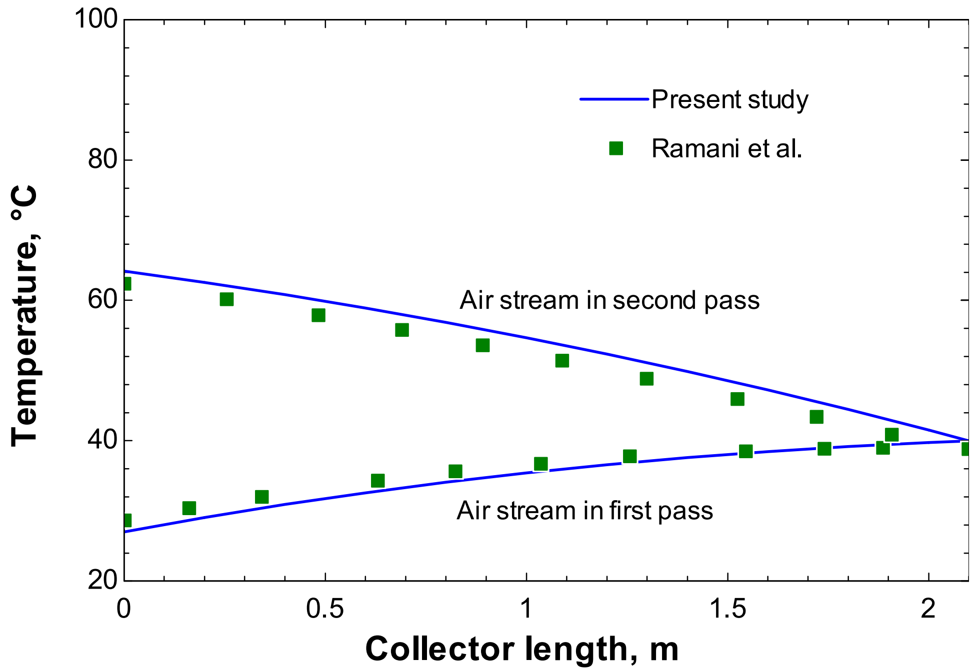

Figure 2. Validation of local air temperatures with the published data [16].

Table 3 presents the range of key parameters that were used to investigate the thermo-hydraulic performance and entropy generation in this study. It should be noted that the case with $y = z = 0$ is the traditional triple-pass collector. This case is considered as the base case for comparison with cases where y or z is greater than zero. For the multi-objective optimization of maximum thermohydraulic efficiency and minimum entropy generation, a genetic algorithm (GA) was adopted. The settings of the GA are provided in Table 4, which were partially adapted to our previous study [29]. The optimum curve can be displayed by means of a Pareto front [30]. To specify the ultimate optimal solution in terms of Pareto optimality, the TOPSIS (Technique for Order of Preference by Similarity to Ideal Solution) decision-making process was adopted. Another common decision-making technique is LINMAP (Linear Programming Technique for Multi-dimensional Analysis of Preference). The LINMAP method chooses the best solution by finding the shortest distance to the ideal point. The TOPSIS is attributed to the better method because the idea of this technique is to seek out the point that is nearest to the ideal point and the furthermost from the non-ideal point [31]. The lengths from a point to the ideal point (l_{i+}) and non-ideal point (l_{i-}) are estimated as [32]:

$$l_{i+} = \sqrt{\left(S_{gen} - S_{gen,ideal}\right)^2 + \left(\eta_{eff} - \eta_{eff,ideal}\right)^2}, \tag{29}$$

$$l_{i-} = \sqrt{\left(S_{gen} - S_{gen,non\text{-}ideal}\right)^2 + \left(\eta_{eff} - \eta_{eff,non\text{-}ideal}\right)^2}. \tag{30}$$

Table 3. Range of key parameters.

Key Parameter	Range
Reynolds number in the third pass	Re_3 = 8000–18,000
Airflow ratio in the second pass	y = 0–0.4
Airflow ratio in the third pass	z = 0–0.4

Table 4. Parameters of the multi-objective optimization genetic algorithm.

Parameter	Value	Remark
Population size	260	Very large population size results in long computation time
Crossover fraction	0.8	Matlab manual and thermal research [33] recommend the value to obtain the best result
Pareto fraction	0.35	Default value
Maximum number of generations	200 × number of variables	Sensitivity analysis revealed that the Pareto frontier is reached after 121 iterations
Mutation function	Adaptive feasible	Due to bounds, used as shown in Table 3
Selection type	Tournament	Enhances chance of selection for the fittest individual [33]
Crossover function	Intermediate	Default crossover function
Population type	Double vector	The individuals owned type double (not string)

To meet the condition of TOPSIS, the ultimate optimal solution has the biggest value of the ratio, as given by:

$$Cl_i = \frac{l_{i-}}{l_{i-} + l_{i+}}. \tag{31}$$

3. Results and Discussion

The influence of key parameters on the thermohydraulic efficiency, entropy generation, and the determination of optimal parameters is presented in this section. Figures 3–8 show the influence of air flow ratios on the thermo-hydraulic parameters and entropy generation at Re_3 = 10,000. The effect of air flow ratios on the temperature difference through the collector is presented in Figure 3. A general trend can be seen that as the ratio increases, the temperature difference decreases. In the base case (y = z = 0), the air temperature difference was the largest. This is because the reduced air flow in passes 1 or 2 decreased the convection heat exchange coefficient, thereby reducing the heat transfer capacity. It can be clearly seen, however, that the reduction of the temperature difference with the flow ratios was not significant. In the case where y = z = 0.4, the air temperature difference was about 0.15 K lower than that of the base case. This was due to the fact that radiant heat transfer existed in the multi-pass air collector. Figure 4 shows the average radiant heat transfer coefficients which were calculated from the average temperature of the surfaces. It is clear that as the Reynolds number increased, the radiant heat transfer coefficient decreased due to a decrease in the surface temperatures. However, at certain Reynolds numbers, all radiant heat transfer coefficients of the three-inlet SAH with airflow ratios of 0.4 were greater than those of the base case. This resulted in a negligible decrease in the air temperature difference with increasing airflow ratios. As the air flow decreased, the temperature of the heat exchanger surfaces increased, thereby increasing the temperature difference between the fluid and the heat transfer surface. The heat transfer rate was proportional to the temperature difference. The temperature distributions of the air flows and heat transfer surfaces are depicted in Figure 5 with respect to the extremes of the airflow ratios (i.e., 0 and 0.4).

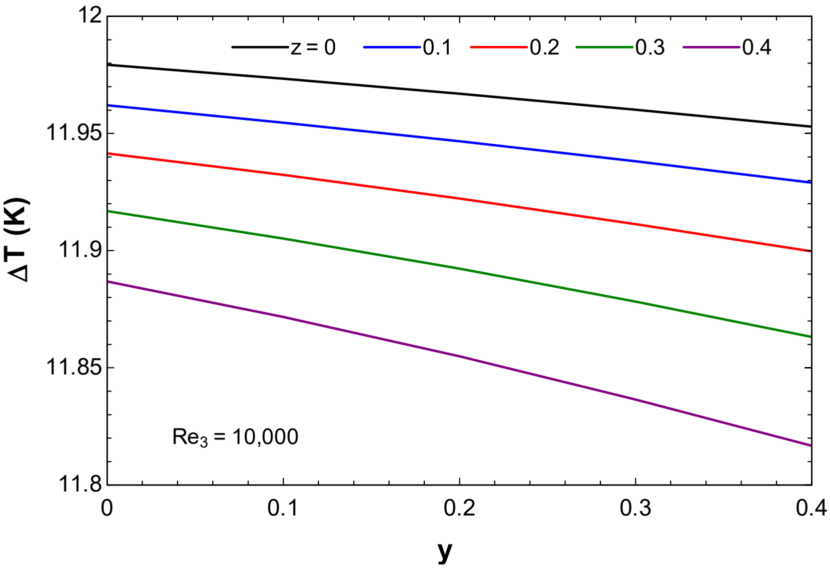

Figure 3. Effect of airflow ratios on temperature increase.

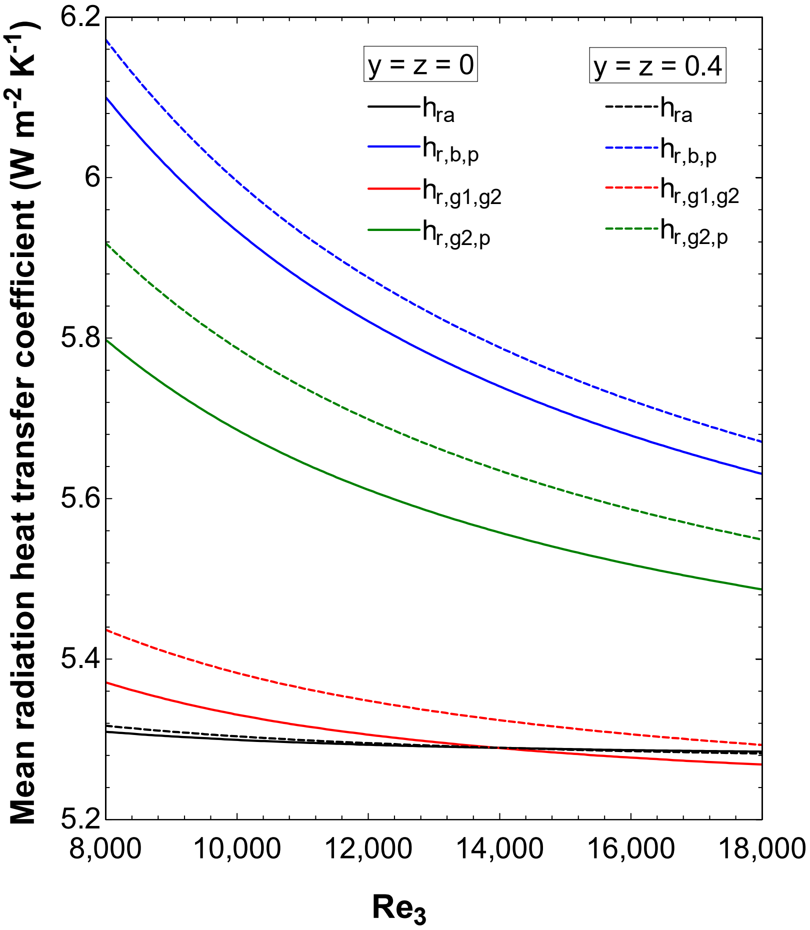

Figure 4. Comparison of the mean radiation heat transfer coefficient for the base case and the case with $y = z = 0.4$.

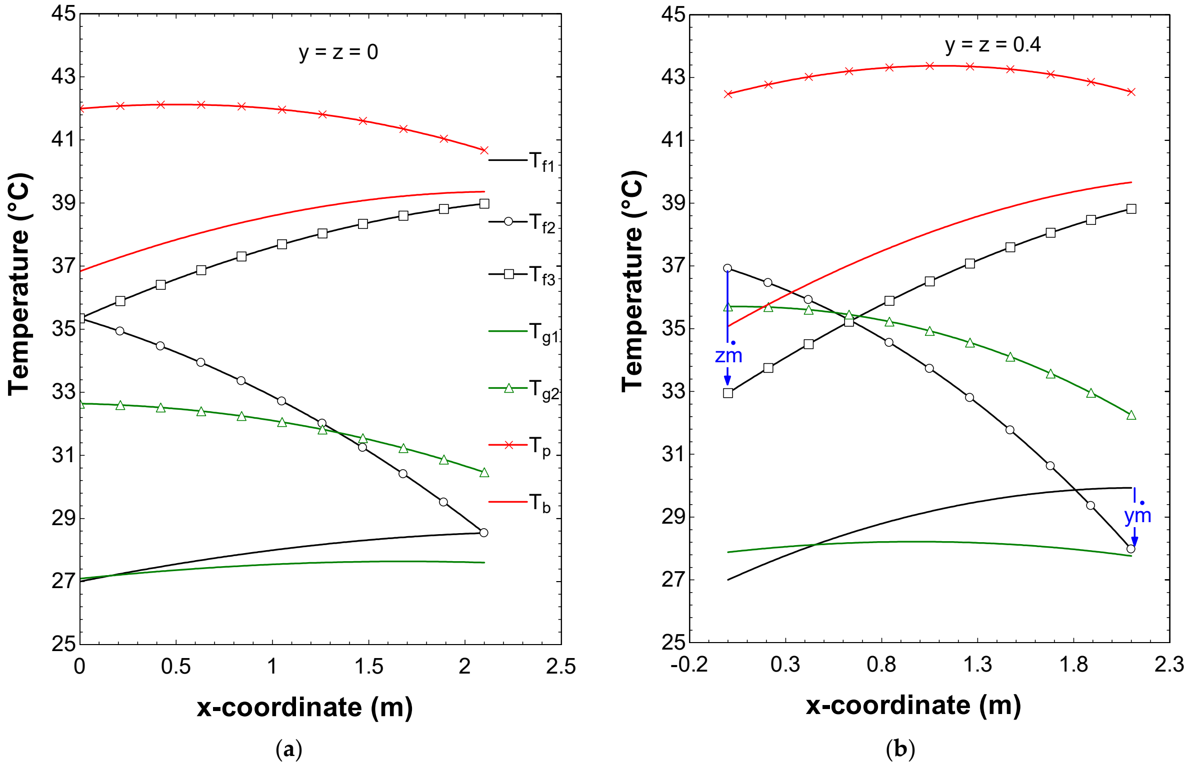

Figure 5. Local temperature of airflow in three passes, i.e., glass covers, absorber plate, and back plate at Re_3 = 10,000: (**a**) $y = z = 0$ (base case) and (**b**) $y = z = 0.4$.

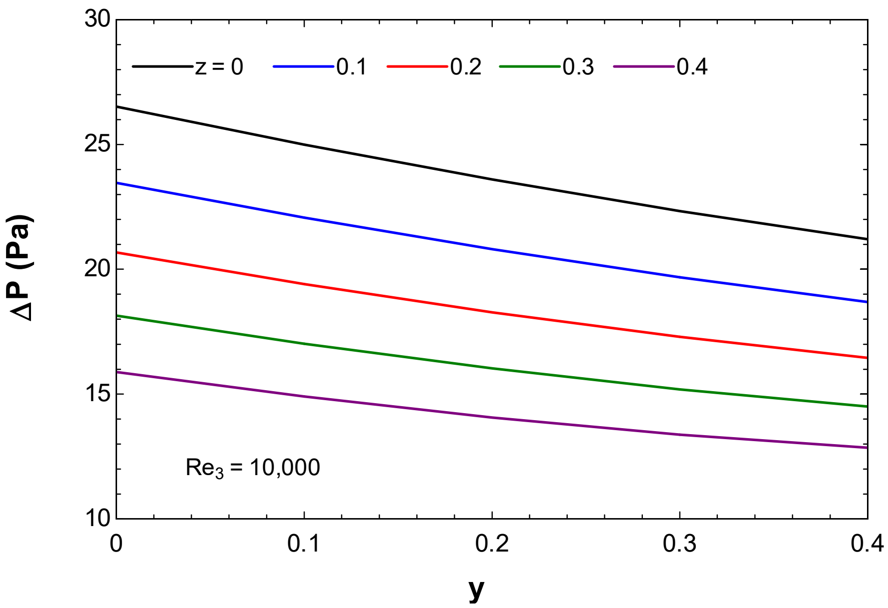

Figure 6. Effect of airflow ratios on pressure difference.

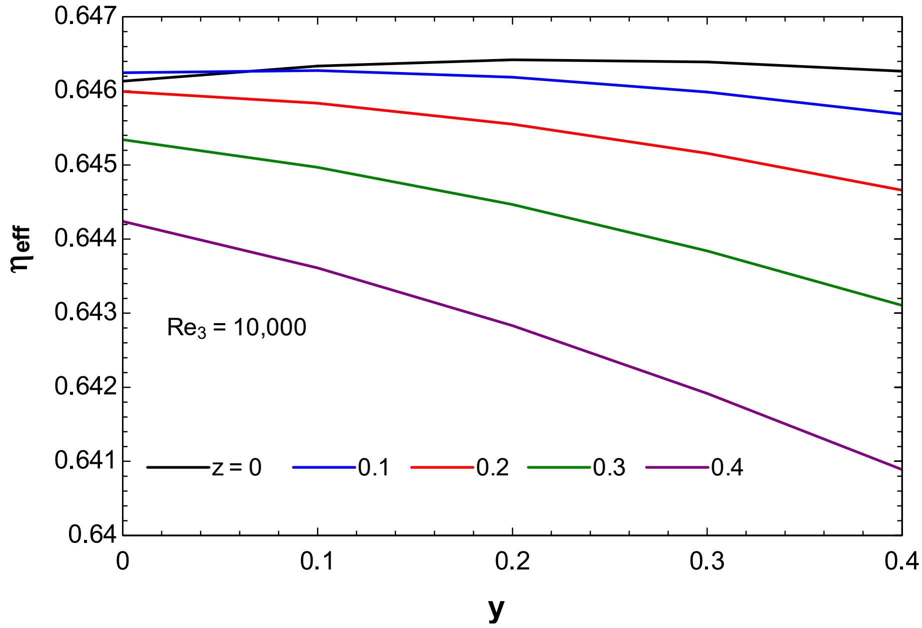

Figure 7. Effect of airflow ratios on thermohydraulic efficiency.

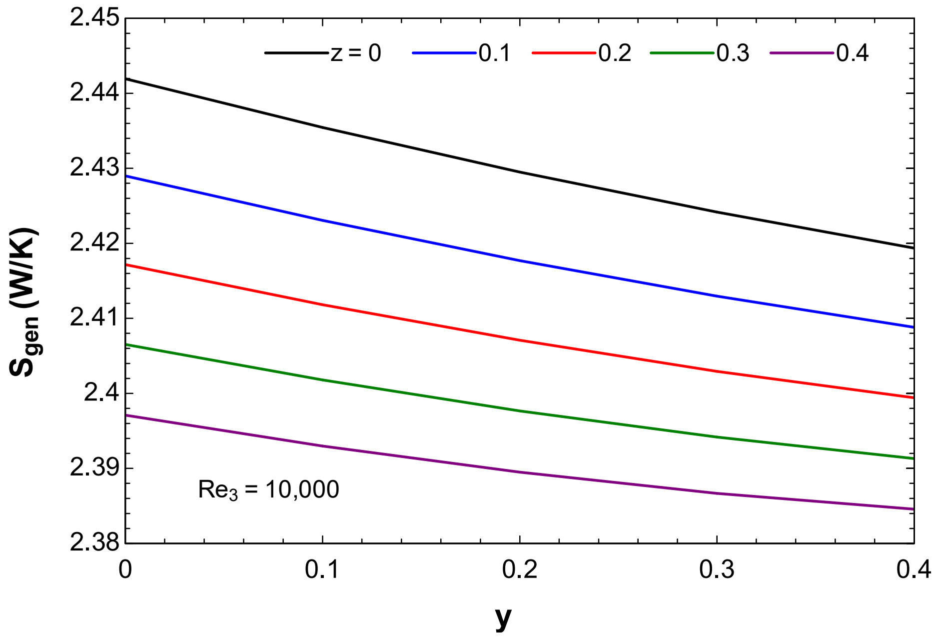

Figure 8. Effect of airflow ratios on entropy generation.

The air temperature increased gradually through the passes. In the case of three inlets (Figure 5b), air temperatures entering the second and third passes were reduced compared to the air temperatures exiting the first and second passes, respectively. The temperatures in the first and second passes were reduced due to the fact that cool ambient air entered the collector from the additional inlets with the airflows of $y\dot{m}$ and $z\dot{m}$, respectively. It is clear that when decreasing the air flow rate of passes 1 and 2, the air temperature difference at these passes increases. The third pass had the same flow rate for both cases in Figure 5. However, the air temperature difference of the third pass in the three-inlet collector was much larger than that of the traditional triple-pass SAH: about 6 K vs. 4 K. This is because the average temperature of the absorber plate of the base case was about 41 °C, while that in the case where $y = z = 0.4$ was about 43 °C. In the base case (Figure 5a), the airflow in the first pass received heat mainly from glass 2. The difference in air temperature through the second pass was the largest, as this was the main pass (i.e., the air exchanged heat with the absorber plate). Hence, the temperature cross occurred between the second pass air temperature (T_{f2}) and temperature of glass 2 (T_{g2}). The absorber plate temperature profile was in line with the second pass air temperature. In the case y = z = 0.4 (Figure 5b), the first pass air received heat from the upper glass until x = 0.5 m, as the lower air flow led to higher glass temperatures. The absorber plate temperature (T_p) reached its maximum in the middle of the collector (x = 1.1 m), as the heat exchange occurring at the second and third passes was almost the same. However, the direction of the temperature rise of these two passes was opposite, such that the absorber plate temperature reached its maximum in the middle of the collector.

The hydraulic loss with flow ratios is shown in Figure 6. It can be clearly observed that the air pressure difference decreased notably with increasing flow ratios: 25.5 Pa in the base case and 13 Pa at y = z = 0.4 (i.e., pressure drop by a half). Figure 7 illustrates the variations of useful heat gain and pumping power, as assessed by thermohydraulic efficiency, with air flow ratios. Taking the aforementioned discussions into account, we determined that the efficiency can reach a maximum at a certain airflow ratio. Greater efficiencies were achieved at flow ratios less than 0.1. This is because the performance of an SAH is dominated by heat transfer compared to pumping power. The thermohydraulic efficiency reached a maximum of 64.65% at z = 0 and y = 0.2. At z = 0.4, the efficiency dropped from 64.42 to 64.08% when increasing y from 0 to 0.4. At y = 0.4, the efficiency decreased from 64.62 to 64.08% as z increased from 0 to 0.4. In other words, the thermohydraulic parameters were affected more strongly by the change of feed air into the third pass. Figure 8 shows the entropy generation with flow ratios. We observed that the entropy generation decreases with the increase of airflow ratios. This behavior results from a change in the airflow ratio, which had little effect on the outlet temperature but greatly reduced the pressure loss. The effect of the irreversibility due to the frictional loss can be expressed by the last term of Equation (27). Entropy generation decreased from 2.442 W/K to 2.384 W/K when increasing flow ratios from 0 to 0.4.

The impacts of the Reynolds number in the third pass (Re_3) and the airflow ratios are shown in Figures 9–12. As the Reynolds number increased, both heat transfer and pressure loss increased. The convection heat transfer coefficient was proportional to the 0.8 power of the Reynolds number (Equation (14)) and the air pumping power was proportional to the 2.75 power of the Reynolds number (Equations (23)–(25)). Hence, the efficiency peaked at some Reynolds number when the ratios were fixed, as seen in Figures 9 and 11. It can be inferred from Figure 9 that the maximum efficiency at each z-value was roughly the same. However, when z was larger, the optimum Re_3 was also greater. At z = 0, the optimal Re number was around 10,000, while the optimal Re number was around 13,000 at z = 0.4. This is a promising outcome in terms of increasing the air flow through the triple-pass collector with additional inlets. In addition, when Re_3 > 11,000, the base case performance was minimal. Entropy generation increased with an increasing Reynolds number and with decreasing flow ratios, as can be observed from Figures 10 and 12. The increase of the entropy generation with the Reynolds number was mainly due to increased pressure loss penalty (ΔP). It can be noticed that the effect of z on the efficiency and entropy generation was more pronounced than that of y, as the third pass was the main heat exchange channel and the pressure loss was the largest for the triple-pass SAH with three inlets. From Figures 9 and 11, it can be concluded that a three-inlet air collector should be used when the Reynolds number is greater than 11,000 in terms of the thermohydraulic performance.

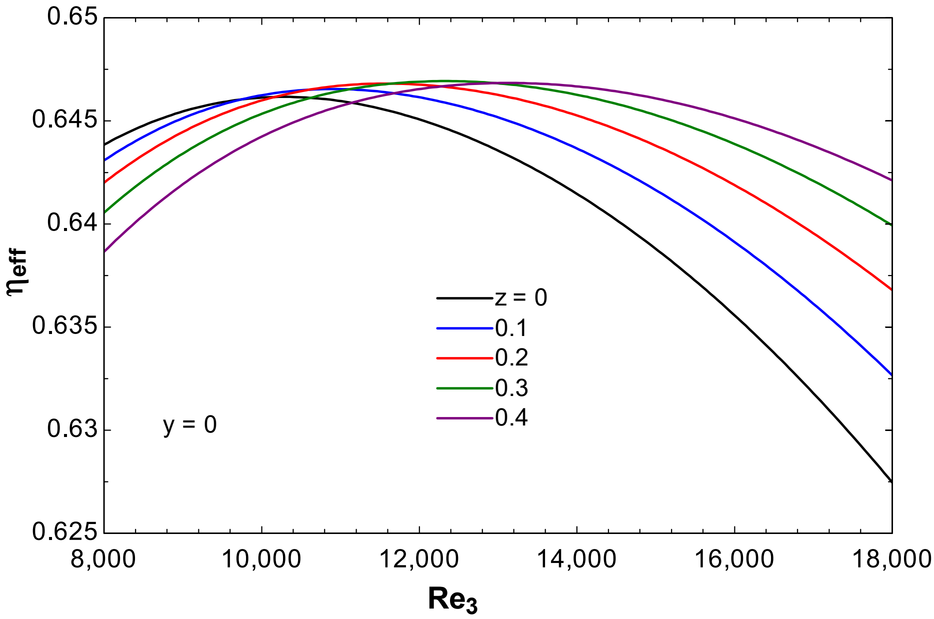

Figure 9. Effect of airflow ratio *z* and Reynolds number on thermohydraulic efficiency.

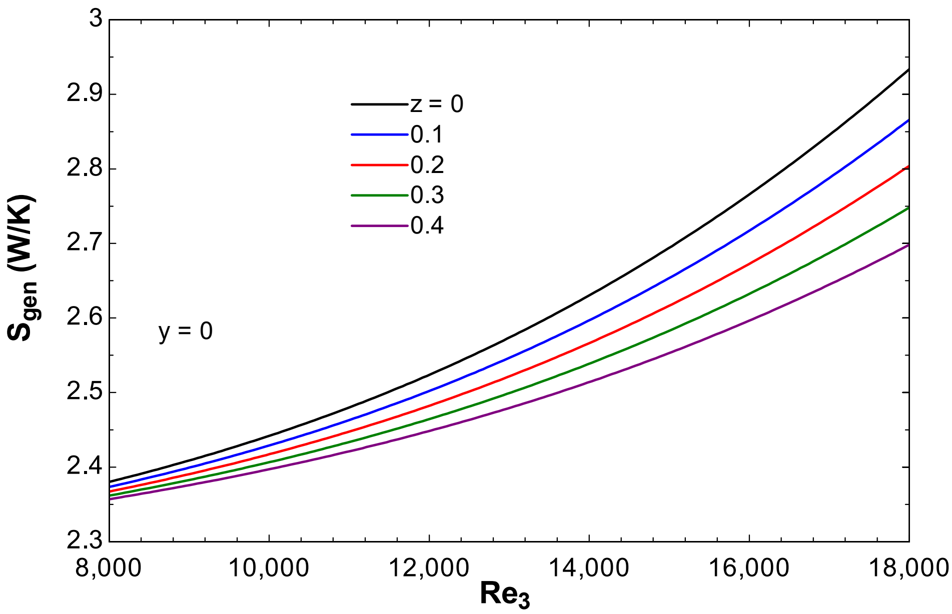

Figure 10. Effect of airflow ratio *z* and Reynolds number on entropy generation.

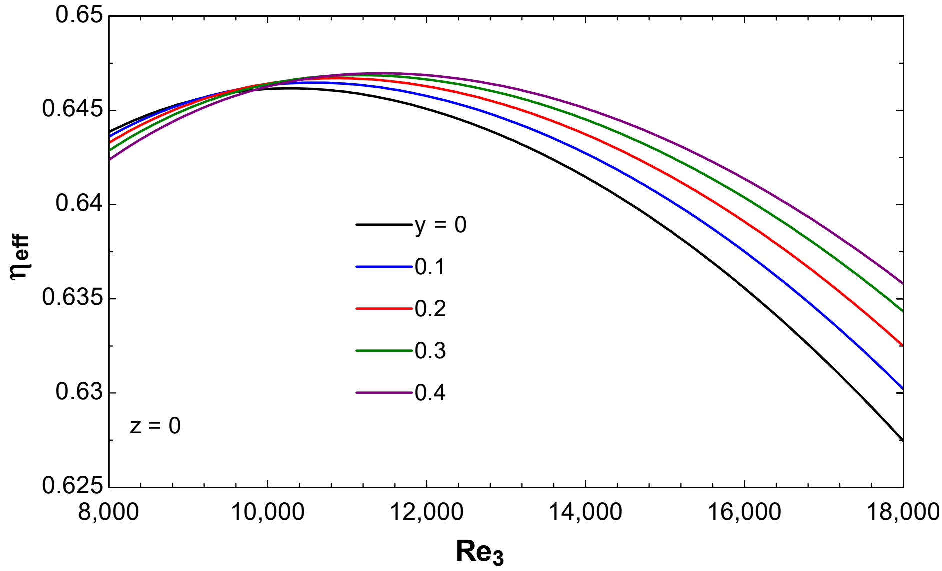

Figure 11. Effect of airflow ratio y and Reynolds number on thermohydraulic efficiency.

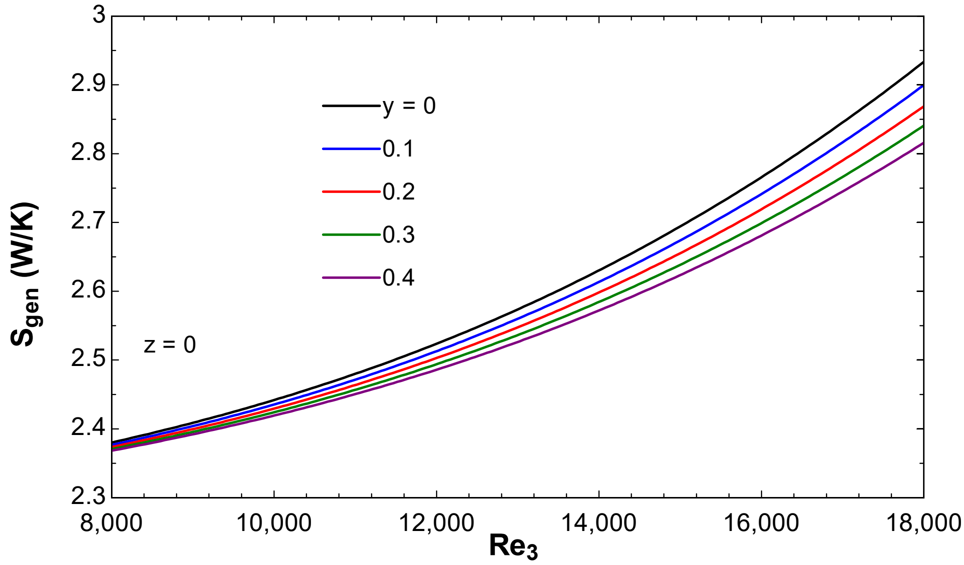

Figure 12. Effect of airflow ratio y and Reynolds number on entropy generation.

From the above parametric study, it can be seen that the Reynolds number and airflow ratios had opposite effects on collector efficiency and entropy generation. The maximum efficiency was achieved at a certain Reynolds number and at certain airflow ratios in the surveyed range. Meanwhile, entropy generation increased with the increase of Re and decrease of flow ratios. Therefore, to assign optimal values of independent parameters, a Pareto front was constructed, as shown in Figure 13. The Pareto front curve was established using the genetic algorithm with the settings shown in Table 4. The curve was a series of optimal solutions that yielded a large efficiency and small entropy generation. Ideal and non-ideal points located at the vertices of the rectangle formed by the Pareto curve were found. To determine the final solution, the TOPSIS decision-making technique was applied, which found S_{gen} = 2.4691 W/K and η_{eff} = 65.38%, as shown in the graph. This is the point that was closest to the ideal point (bottom-right corner) and furthest from the non-ideal point (top-left corner). The optimal parameters at the selected point were found to be Re_3 = 11,156, y = 0.258, and z = 0.036. In addition, Figure 13 also shows the maximum efficiency value corresponding to the maximum entropy generation and vice versa.

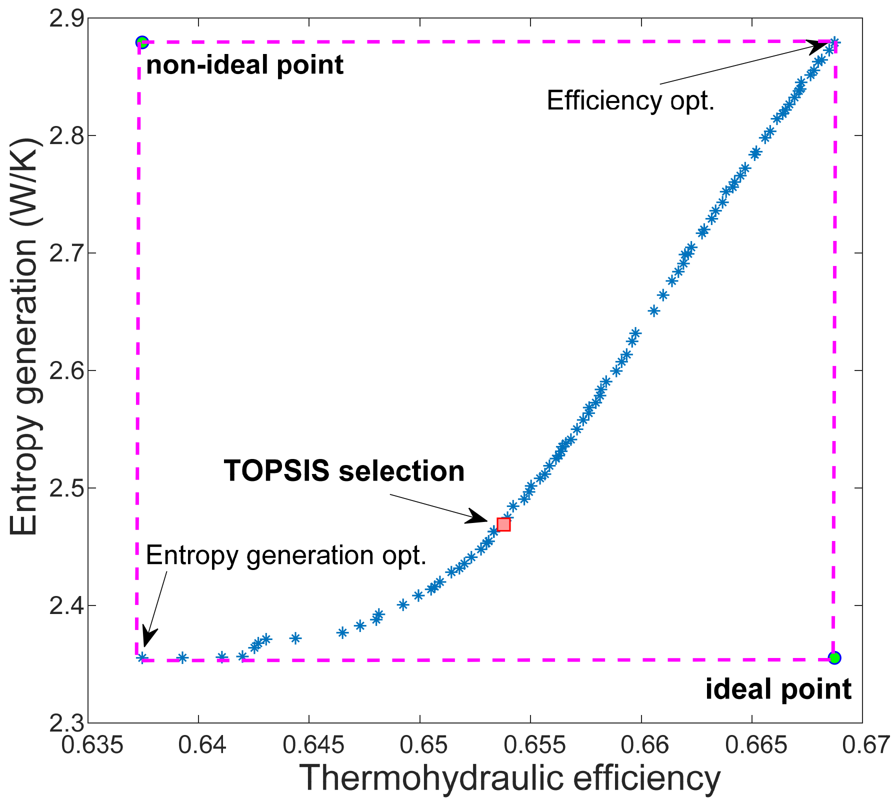

Figure 13. Pareto front and ultimate optimum solution selected by TOPSIS decision-making process.

4. Conclusions

A one-dimensional analytical model was formed to evaluate the temperature distribution in a three-inlet triple-pass solar air heater. Thermohydraulic efficiency and entropy generation served as the criteria to estimate its performance when changing the Reynolds number of the air in the third pass and in the airflow ratio of the inlets. The thermohydraulic performance and entropy generation were significantly improved by adding inlets when the collector operated with a high airflow. The main findings of the present research study are as follows:

1. The air temperature difference showed little change with the airflow ratios. However, the pressure loss of the three-inlet triple-pass SAH was reduced to half of that of the traditional triple-pass SAH.
2. Thermohydraulic efficiency reached high values when the airflow ratios were less than 0.1.
3. Increasing the airflow ratio increased the optimal Reynolds number for maximum thermohydraulic efficiency.
4. When the Reynolds number was greater than 11,000, the performance of the three-inlet triple-pass SAH was greater than that of the traditional triple-pass SAH.
5. Increasing the Reynolds number and decreasing the airflow ratios increased entropy generation.
6. The influence of the third pass airflow ratio on the thermal–hydraulic parameters and entropy generation was more pronounced than that of the airflow ratio of the second pass.
7. Re_3 = 11,156, y = 0.258, and z = 0.036 are the optimal values for maximum thermohydraulic efficiency and minimum entropy generation.

Author Contributions: Conceptualization, N.M.P.; investigation, N.T.T., N.V.H. and N.M.P.; methodology, N.M.P.; software, N.T.T. and N.M.P.; supervision, N.M.P.; validation, N.T.T.; visualization, N.V.H.; writing—original draft preparation, N.T.T. All authors have read and agreed to the published version of the manuscript.

Funding: Not applicable.

Institutional Review Board Statement: Not applicable.

Informed Consent Statement: Not applicable.

Data Availability Statement: Not applicable.

Acknowledgments: We would like to thank the Industrial University of Ho Chi Minh City (IUH) and Ho Chi Minh City University of Technology (HCMUT), VNU-HCM, for their time, support, and facilities for this study.

Conflicts of Interest: The authors declare no conflict of interest.

Nomenclature

A_c	area of absorber plate (m^2)
c_p	specific heat at a constant pressure ($Jkg^{-1}K^{-1}$)
D	channel depth (m)
D_e	hydraulic diameter (m)
f	friction factor
h	heat transfer coefficient ($Wm^{-2}K^{-1}$)
I	solar radiation (W/m^2)
k	thermal conductivity ($Wm^{-1}K^{-1}$)
L	collector length (m)
$\dot{m}$	air mass flow rate (kg/s)
n	number of fins
P	pressure (Pa)
Pr	Prandtl number
Q	heat transfer rate (W)
Re	Reynolds number
S_{gen}	entropy generation (W/K)
t	fin thickness (m)
T	temperature (K)
V	velocity (m/s)
W	collector width (m)
W_f	fin height (m)
x	coordinator (m)
y	airflow ratio of the second pass, $0 \leq y < 1$
z	airflow ratio of the third pass, $0 \leq z < 1$
Greek symbols	
α	absorptivity
Δ	difference
ε	emissivity
η	efficiency
μ	dynamic viscosity (Pa.s)
ϕ	area-weighted fin efficiency
ρ	air density (kg/m^3)
σ	Stefan constant
τ	transmissivity
Subscripts	
a	ambient
b	back plate
c	convection
Eff	thermohydraulic
f	fluid (Air), fin

g	glass cover
o	outlet
p	absorber plate
r	radiation
s	sun
w	wind

References

1. Farjana, S.H.; Huda, N.; Mahmud, M.A.P.; Saidur, R. Solar process heat in industrial systems—A global review. *Renew. Sust. Energ. Rev.* **2018**, *82*, 2270–2286. [CrossRef]
2. Phu, N.M.; Luan, N.T. A review of energy and exergy analyses of a roughened solar air heater. *J. Adv. Res. Fluid Mech. Therm. Sci.* **2021**, *77*, 160–175.
3. Thao, P.B.; Truyen, D.C.; Phu, N.M. CFD Analysis and Taguchi-Based Optimization of the Thermohydraulic Performance of a Solar Air Heater Duct Baffled on a Back Plate. *Appl. Sci.* **2021**, *11*, 4645. [CrossRef]
4. Nguyen Thanh, L.; Nguyen Minh, P. First and Second Law Evaluation of Multipass Flat-Plate Solar Air Collector and Optimization Using Preference Selection Index Method. *Math. Probl. Eng.* **2021**, *2021*, 5563882.
5. Chamoli, S.; Chauhan, R.; Thakur, N.; Saini, J. A review of the performance of double pass solar air heater. *Renew. Sust. Energ. Rev.* **2012**, *16*, 481–492. [CrossRef]
6. Tuncer, A.D.; Sözen, A.; Khanlari, A.; Amini, A.; Şirin, C. Thermal performance analysis of a quadruple-pass solar air collector assisted pilot-scale greenhouse dryer. *Sol. Energy* **2020**, *203*, 304–316. [CrossRef]
7. Khanlari, A.; Sözen, A.; Afshari, F.; Şirin, C.; Tuncer, A.D.; Gungor, A. Drying municipal sewage sludge with v-groove triple-pass and quadruple-pass solar air heaters along with testing of a solar absorber drying chamber. *Sci. Total Environ.* **2020**, *709*, 136198. [CrossRef]
8. Kesavan, S.; Arjunan, T.; Vijayan, S. Thermodynamic analysis of a triple-pass solar dryer for drying potato slices. *J. Therm. Anal. Calorim.* **2019**, *136*, 159–171. [CrossRef]
9. Sopian, K.; Alghoul, M.; Alfegi, E.M.; Sulaiman, M.; Musa, E. Evaluation of thermal efficiency of double-pass solar collector with porous–nonporous media. *Renew. Energy* **2009**, *34*, 640–645. [CrossRef]
10. Ho, C.-D.; Lin, C.-S.; Chuang, Y.-C.; Chao, C.-C. Performance improvement of wire mesh packed double-pass solar air heaters with external recycle. *Renew. Energy* **2013**, *57*, 479–489. [CrossRef]
11. Yeh, H.-M.; Ho, C.-D. Collector efficiency in downward-type internal-recycle solar air heaters with attached fins. *Energies* **2013**, *6*, 5130–5144. [CrossRef]
12. Singh, S.; Dhiman, P. Analytical and experimental investigations of packed bed solar air heaters under the collective effect of recycle ratio and fractional mass flow rate. *J. Energy Storage* **2018**, *16*, 167–186. [CrossRef]
13. Ho, C.-D.; Chang, H.; Hsiao, C.-F.; Huang, C.-C. Device performance improvement of recycling double-pass cross-corrugated solar air collectors. *Energies* **2018**, *11*, 338. [CrossRef]
14. Abo-Elfadl, S.; Yousef, M.S.; Hassan, H. Assessment of double-pass pin finned solar air heater at different air mass ratios via energy, exergy, economic, and environmental (4E) approaches. *Environ. Sci. Pollut. Res.* **2021**, *28*, 13776–13789. [CrossRef]
15. Ahmadkhani, A.; Sadeghi, G.; Safarzadeh, H. An in depth evaluation of matrix, external upstream and downstream recycles on a double pass flat plate solar air heater efficacy. *Therm. Sci. Eng. Prog.* **2021**, *21*, 100789. [CrossRef]
16. Ramani, B.; Gupta, A.; Kumar, R. Performance of a double pass solar air collector. *Sol. Energy* **2010**, *84*, 1929–1937. [CrossRef]
17. Tan, H.M.; Charters, W.W.S. Effect of thermal entrance region on turbulent forced-convective heat transfer for an asymmetrically heated rectangular duct with uniform heat flux. *Sol. Energy* **1969**, *12*, 513–516. [CrossRef]
18. Sahu, M.K.; Sharma, M.; Matheswaran, M.; Maitra, K. On the use of longitudinal fins to enhance the performance in rectangular duct of solar air heaters—A review. *J. Sol. Energy Eng.* **2019**, *141*, 030802. [CrossRef]
19. Velmurugan, P.; Kalaivanan, R. Thermal performance studies on multi-pass flat-plate solar air heater with longitudinal fins: An analytical approach. *Arab. J. Sci. Eng.* **2015**, *40*, 1141–1150. [CrossRef]
20. Naphon, P. On the performance and entropy generation of the double-pass solar air heater with longitudinal fins. *Renew. Energy* **2005**, *30*, 1345–1357. [CrossRef]
21. Phu, N.M.; Van Hap, N. Performance Evaluation of a Solar Air Heater Roughened with Conic-Curve Profile Ribs Based on Efficiencies and Entropy Generation. *Arab. J. Sci. Eng.* **2020**, *45*, 9023–9035. [CrossRef]
22. Phu, N.M.; Bao, T.T.; Hung, H.N.; Tu, N.T.; Van Hap, N. Analytical predictions of exergoeconomic performance of a solar air heater with surface roughness of metal waste. *J. Therm. Anal. Calorim.* **2021**, *144*, 1727–1740. [CrossRef]
23. Fudholi, A.; Sopian, K. A review of solar air flat plate collector for drying application. *Renew. Sust. Energ. Rev.* **2019**, *102*, 333–345. [CrossRef]
24. Muñoz, M.; Roa, M.; Correa, R. Entropy generation analysis for the design of a flat plate solar collector with fins. *Dyna* **2020**, *87*, 199–208. [CrossRef]
25. Phu, N.M.; Lee, G.S. Characteristics of pressure and force considering friction in a closed cylinder with a holed piston. *J. Mech. Sci. Technol.* **2014**, *28*, 2409–2415. [CrossRef]
26. Klein, S.A. *Engineering Equation Solver (EES)*; F-Chart Software: London, UK, 2013.

27. Nellis, G.; Klein, S. *Heat Transfer*; Cambridge University Press: New York, NY, USA, 2009; pp. 317–348.
28. Abuşka, M.; Şevik, S. Energy, exergy, economic and environmental (4E) analyses of flat-plate and V-groove solar air collectors based on aluminium and copper. *Sol. Energy* **2017**, *158*, 259–277. [CrossRef]
29. Thao, P.B.; Phu, N.M.; Truyen, D.C. Comparative Study and Optimization of CO_2 Capture and Storage in LNG-fired Power Plant. *J. Adv. Res. Fluid Mech. Therm. Sci.* **2020**, *72*, 55–66.
30. Zhou, T.; Nguyen, V.H.; Lee, G.S. Design optimization of heat exchangers for solar-heating ocean thermal energy conversion (SH-OTEC) using high-performance commercial tubes. *Trans. Korean Soc. Mech. Eng. B* **2016**, *40*, 557–567. [CrossRef]
31. Alhamid, M.I.; Aisyah, N. Exergetic-Economic analysis and optimization of solar assisted heat pump using Multi-objective Genetic Algorithm. *IOP Conf. Ser. Earth Environ. Sci.* **2018**, *105*, 012064.
32. Tuyen, V.; Van Hap, N.; Phu, N.M. Thermal-hydraulic characteristics and optimization of a liquid-to-suction triple-tube heat exchanger. *Case Stud. Therm. Eng.* **2020**, *19*, 100635. [CrossRef]
33. Imran, M.; Pambudi, N.A.; Farooq, M. Thermal and hydraulic optimization of plate heat exchanger using multi objective genetic algorithm. *Case Stud. Therm. Eng.* **2017**, *10*, 570–578. [CrossRef]